Microstructure of Surface and Subsurface Layers of a Ni-Ti Shape Memory Microwire

H. Tian,[1] D. Schryvers,[1,*] S. Shabalovskaya,[2,†] and J. Van Humbeeck[2]

[1]EMAT, University of Antwerp, Groenenborgerlaan 171, B-2020 Antwerp, Belgium
[2]MTM, K.U. Leuven, Kasteelpark Arenberg, B-3001 Leuven, Belgium

Abstract: The microstructure of a 55 μm diameter, cold-worked Ni-Ti microwire is investigated by different transmission electron microscopy techniques. The surface consists of a few hundred nanometer thick oxide layer composed of TiO and TiO_2 with a small fraction of inhomogeneously distributed Ni. The interior of the wire has a core-shell structure with primarily B2 grains in the 1 μm thick shell, and heavily twinned B19′ martensite in the core. This core-shell structure can be explained by a concentration gradient of the alloying elements resulting in a structure separation due to the strong temperature dependence of the martensitic start temperature. Moreover, in between the B2 part of the metallic core-shell and the oxide layer, a Ni_3Ti interfacial layer is detected.

Key words: nickel-titanium microwire, TEM, shape memory, surface modification, composition gradient, surface oxide, rutile, Ni release, EELS

INTRODUCTION

Due to its unique mechanical properties including shape memory and superelasticity, its durability and biocompatibility, applications of Nitinol for a wide variety of medical implants and devices are progressively increasing (Ryhänen, 1999; Shabalovskaya, 2001, 2002; Kujala et al., 2004). However, as Nitinol consists of about 50 at.% Ni, certain applications are still hindered by the concern of Ni release in the surrounding tissue. The biocompatibility of Ni-Ti implants is essentially guaranteed by a corrosion resistant and biologically inert titanium oxide layer avoiding severe toxicological and allergic responses to the Ni (Shabalovskaya, 1996). The structure of this layer can be controlled by various thermomechanical surface treatments (Shabalovskaya, 1996, 2002). Due to the present day miniaturization of Nitinol devices, concerns with their corrosion and fracture, and especially Ni release in the body, are worsening. Although the titanium oxide layer is formed spontaneously on the Nitinol surface, reports on the increase of Ni release with time (up to 6 months) are multiplying (Cisse et al., 2002; Kobayashi et al., 2005; Clarke et al., 2006; Sui & Cai, 2006). These new patterns in Ni release are different from those observed traditionally when the release was reduced to undetectable levels after 10–14 days of exposure of Nitinol

(Wever et al., 1998; Michiardi et al., 2006; Ryhänen et al., 1997). For the moment there is no explanation for the controversies in the behavior of Ni release. However, Ni release that may be extended to a few months in the body would significantly alter the healing patterns of tissues surrounding the Ni-Ti implants. The unexplained cases of abnormal bone remodeling (Berger-Gorbet et al., 1996; Takeshita et al., 1997) and the problem with neointimal proliferation (Bayer & Roguin, 1997; Roguin et al., 1999; Kobayashi et al., 2001) a few months after Nitinol implantation could easily be attributed to a lasting Ni release.

Although there are a number of studies on the chemistry and structure of surface sublayers of Nitinol that underwent various heat treatments, the exact mechanisms of formation of various Ni_xTi_y phases and types of metal diffusion in the surface and interior are not clear. This is especially true when considering Nitinol treated in various media and temperatures. The goal of the present study is to evaluate surface conditions of a Nitinol microwire produced by cold-work assisted by intermediate annealings, the expected materials starting condition for most applications of these wires. This is the first study in a series supported by focused ion beam (FIB) thinning to shed light on the troubling issues associated with the Ni accumulation on the surface and related Ni release. The microstructure of the surface and interior of the microwire are investigated by different transmission electron microscopy (TEM) techniques. The TEM sample preparation via FIB technique allows us to characterize both the near surface as well as the interior bulk structure in a systematic way.
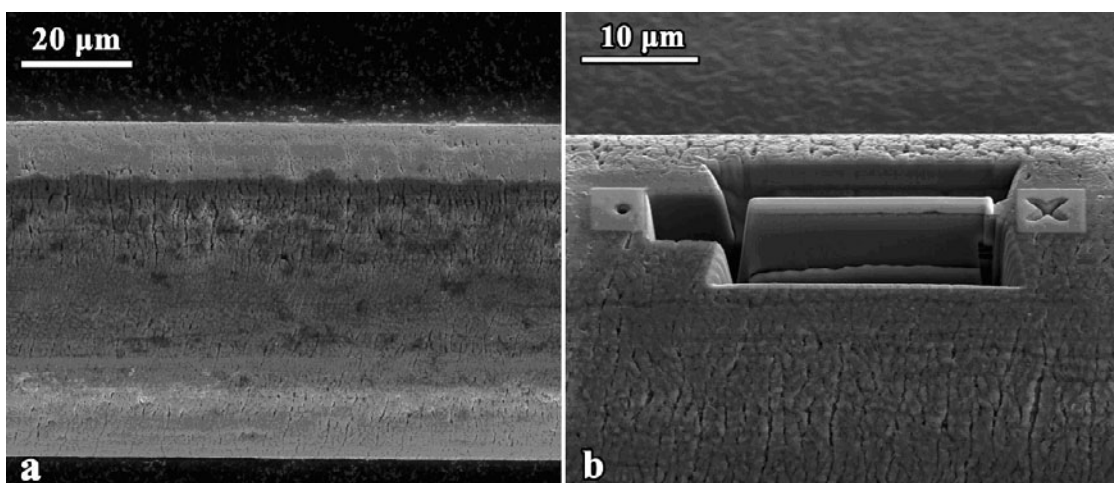
Figure 1. a: SEM image of the wire taken in a dual-beam FIB. **b:** TEM cross section manufactured by FIB at the surface of microwire

MATERIALS AND METHODS

The 55 μm diameter wire, purchased from Memory Metalle (Germany), is 30% cold-worked after wire drawing and has a nominal composition of 49.48 at.% Ni–50.52 at.% Ti. Its fracture stress is 1,360 MPa while the fracture strain is about 4%. No phase transformation is observed by DSC when heating and cooling between $-50°$C and $+150°$C.

Conventionally, metallic samples for TEM are prepared by electropolishing or occasionally by ion milling thin slice cuts from the bulk metal. However, in the present case of a wire with a diameter of only 55 μm, as shown in the scanning electron microscope (SEM) image of Figure 1a, these conventional techniques are hard to apply, plus they will destroy any site-specific information. Thus, an FEI FIB/SEM xT Nova Nanolab 200 was employed, which combines an SEM with a Ga$^+$ ion beam etching column. With this instrument, site-specific TEM samples from micronsized areas as required in the present case can be obtained.

TEM specimens were prepared following the *in situ* lift-out method by removing material from both sides of the desired cross section, as shown in Figure 1b (in the present article only results from cuts parallel to the long axis of the wire are presented). To prevent damaging the surface with the Ga$^+$ ions, the area of interest is covered *in situ* with a protective platinum layer prior to FIB cutting, which can be recognized as the smooth white-grey layer on top of the central cut in Figure 1b. After cutting, the slice of ~15 μm wide, 5 μm deep, and 200 nm thick is cut free, fastened to a needle with Pt deposition and transported and fastened to a modified TEM grid. For regular cutting and thinning, the Ga$^+$ ions are accelerated by 30 kV; while for final thinning to electron transparency (60 nm), the accelerating voltage is reduced to 5 kV. By adjusting the angle of the incident ion beam, a large-scale (3–5 μm) uniformly thin region can be achieved. Alternatively, after fine polishing, some parts of the specimen can be thinned enough ($<$20 nm) to allow high-resolution (HR) TEM imaging. Unfortunately, despite the use of relatively low voltages during the final thinning steps, the Ga$^+$ ion beam still introduces some local damage of the sample, especially at boundaries and interfaces as observed in some of the HRTEM images.

By using the site specificity of the FIB method, samples containing the oxide layer plus the first few microns of the Ni-Ti material (as in Fig. 1b) have been prepared. Also samples from the interior of the wire have been made by first cutting the wire at an inclined angle with a sharp metal knife creating an inclined free surface with exposed interior material. FIB samples are then produced along this freshly inclined surface perpendicular to the central axis of the wire at different depths of the wire.

The TEM observations and energy dispersive X-ray (EDX) measurements were performed in a CM20 Philips instrument equipped with a thin window INCA x-sight EDX detector. HRTEM images and electron energy-loss spectroscopy (EELS) studies were performed in an Ultra-Twin CM30 Philips FEG instrument equipped with a post-column GIF200 detector. EDX quantification was done with the company-provided Cliff-Lorimer thin ratio section software (INCA) in which absorption and fluorescence were ignored under the assumption of a thin foil. EELS quantification was performed in Digital Micrograph® via a sequence of background removals to separate the element-specific excitation from the nonspecific background, multiple scattering removal by deconvolution with the zero-loss (ZL) spectrum, and conversion to chemical concentrations by using the appropriate single-scattering ionization cross sections. To improve the precision and spatial localization, the EELS analysis was performed in diffraction mode using 5–10 nm probes providing a relatively large amount of counts. For each new spectrum from a different region, a
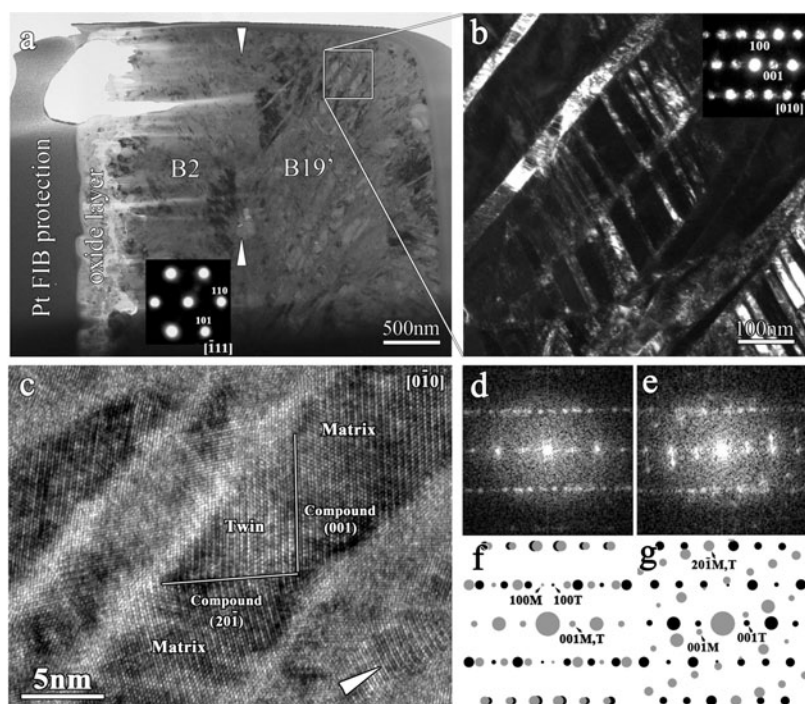
Figure 2. (**a**) Bright field image of both the near-surface oxide and bulk of a microwire, (**b**) dark-field image corresponding to the square area in **a** (nanoprobe electron diffraction patterns of B2 [111] zone axis and martensite B19′ [010] zone axis are inserted in **a** and **b**, respectively). (**c**) HRTEM of nanoscale twin structures of B19′ martensite in the core. FFTs of (**d**) compound (001) and (**e**) (20$\bar{1}$) twins in **c** (location as labeled on HRTEM). The simulated diffraction patterns based on twinning modes of **f** compound (001) and **g** (20$\bar{1}$) twins.

separate ZL was recorded, both with a dispersion of 0.20 eV/pixel. In some cases the details of the energy-loss-near-edge-structure (ELNES) are used to discriminate between similar compounds, in which cases a dispersion of 0.05 eV/pixel was used.

RESULTS

TEM Overview

In Figure 2a both the surface oxide and the first few microns of the bulk of the microwire are recognized. The protective Pt layer is deposited in the FIB to protect the surface oxide from Ga$^+$ damage during TEM sample preparation. The thickness of the oxide layer varies from 100 to 400 nm.

In the bulk of the microwire, a characteristic morphology is observed: a nearly straight boundary (indicated by two arrows) around 1 μm underneath the oxide layer divides the bulk into two structures. One part (left side of the boundary in Fig. 2a) is predominantly austenite B2, as can be concluded from diffraction shown in Figure 2a (inset). This layer also contains a small fraction of B19′ martensite. The other part of the bulk (right side of the boundary) consists of twin structures of B19′ as shown in the dark field image in Figure 2b, revealing a characteristic image of layers-within-layers of twin structures. The corresponding diffraction pattern of one of the larger twin variants is shown in Figure 2b (inset), from which a monoclinic angle $\beta = 82°$ can be measured. As a result, the metallic part of

the wire can be characterized as a twinned B19′ martensite core surrounded by a 1 μm thick B2 shell.

Figure 2c is an HRTEM image of the B19′ core revealing grains containing several types of twins. For example, compound (001) and (20$\bar{1}$) twins are recognized from their respective fast Fourier transforms (FFT) and corresponding simulated diffraction patterns, shown in Figure 2d–g. Furthermore, due to high residual strain fields in the wire, bent lattice planes are observed as indicated by the white arrowhead in Figure 2c. Also, the two twin-related patterns in Figure 2e,g are rotated by a few degrees relative to one another, which again must be attributed to severe deformation. The strong differences in contrast between the inside of the grains and the interfaces in Figure 2c could be an indication of radiation damage from the Ga$^+$ ions at the interfaces containing weaker bonds, despite the protective Pt layer.

Oxide Layer

EDX spectroscopy (EDXS) and EELS reveal that the oxide is predominantly Ti and O, with a small fraction of Ni (<5 at.% with strong local variations). The selected area electron diffraction (SAED) pattern of the oxide (Fig. 3a) indicates that it is a combination of small grains of TiO and TiO$_2$. The interplanar distances for the crystalline phases of TiO$_2$, rutile and anatase, are relatively close (difference below 10%); hence, it is difficult to determine which phase is in the oxide layer by SAED only showing ill-defined ring patterns from small grains.
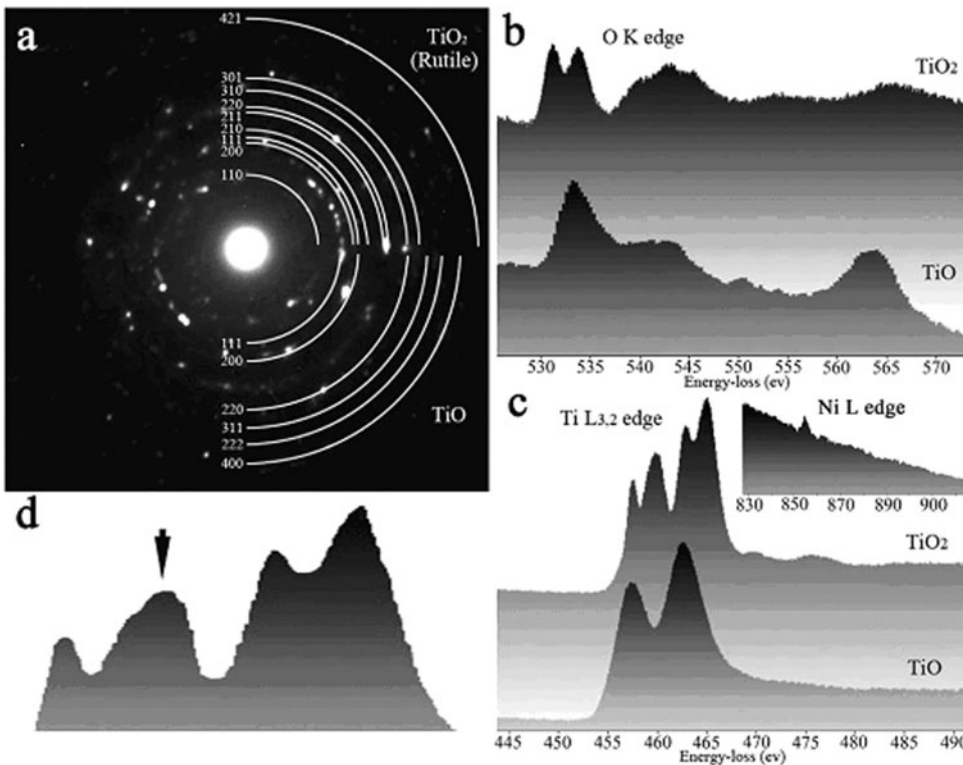
Figure 3. (**a**) SAED pattern of the oxide layer. Nanoprobe ELNES of (**b**) O K and (**c**) Ti $L_{2,3}$ edges as recorded from different nanoscale grains; (**d**) the partially enlarged Ti $L_{2,3}$ ELNES of TiO_2 showing the rutile type.

ELNES of the O, Ti, and Ni edges are shown in Figure 3b,c. Both profiles of O K and Ti $L_{2,3}$ edges in the surface oxide closely resemble those of standard TiO and TiO_2 spectra (Brydson et al., 1989, 1991). Data from different grains reveal the oxide consists of either 51 at.% Ti, 49 at.% O (± 2 at.%), or 33 at.% Ti, 67 at.% O (± 3 at.%), confirming the stoichiometric values for TiO and TiO_2. The inset of Figure 3c shows the Ni L edge at 854 eV, which although too weak for proper quantification, confirms the existence of Ni in the oxide layer.

As shown before (Potapov & Schryvers, 2004), the Ti L edges of rutile and anatase are placed at almost the same energy while the onset of TiO is shifted to a slightly lower energy (by about 0.5 to 2 eV depending on the method chosen for defining the edge onset). Rutile and anatase, however, can only be differentiated in EELS by a small difference in the shape of the second peak of the Ti L_3 edge (rutile peak leans right, anatase peak leans left) and the O K edge ELNES (Brydson et al., 1991; Potapov et al., 2007). Both the O K and Ti $L_{2,3}$ ELNES of the TiO_2 spectra from this specimen show the rutile signature as shown in Figure 3b,d, respectively, confirming earlier results from conventional wires (Potapov et al., 2007).

Bulk of Nitinol Microwire

Energy Dispersive X-Ray Spectroscopy

The content of titanium and nickel may depend on the depth from the surface to the center of the microwire; hence, quantitative EDXS is used to measure the average percentage of titanium and nickel in different depths underneath the oxide layer.

As shown in the cross-sectional TEM image (Fig. 4a), six different depths were analyzed from the bulk. The dashed line indicates the boundary between the B2 shell and B19′ core, as mentioned above. The contrast change across this boundary is caused by changing diffraction conditions. Care was taken to select an area with a constant thickness as determined via the log-ratio method using the zero-loss and plasmon peaks of the corresponding EELS spectrum (Egerton, 1996). A series of five EDX spectra from each depth was measured and the corresponding composition calculated. The average composition and standard deviation for each depth are plotted in Figure 4b.

Quantitative analysis of the EDXS reveals the compositions underneath the B2-B19′ boundary, i.e., in the bulk part, are approximately constant (50.1 at.% Ni–49.9 at.% Ti, ± 0.2 at.%), while an increase in Ni is observed when moving from the boundary toward the surface. The near-surface areas appear to be enriched in Ni, varying from 50.3 to 51.0 at.% Ni, as shown in Figure 4b, be it with a larger standard deviation up to 0.6 at.% for the outer location. The relatively large standard deviations in the "B2" region are primarily due to the unavoidable inclusion of some remaining B19′ grains with a lower Ni content (which also slightly shifts the average to a slightly lower value for Ni in this area).
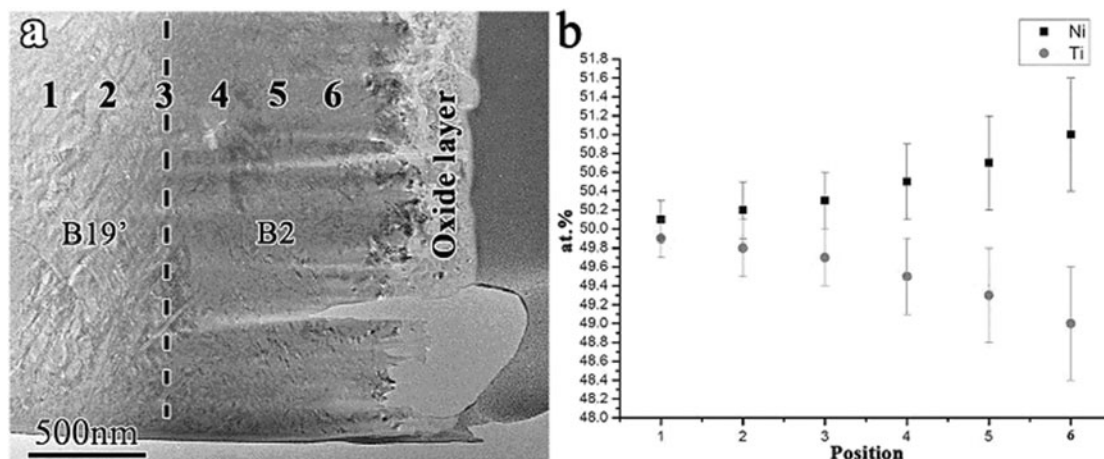
Figure 4. a: TEM image of a cross section of the microwire. **b:** Schematic of the average Ni and Ti contents at different spot locations in the wire as determined by EDXS.
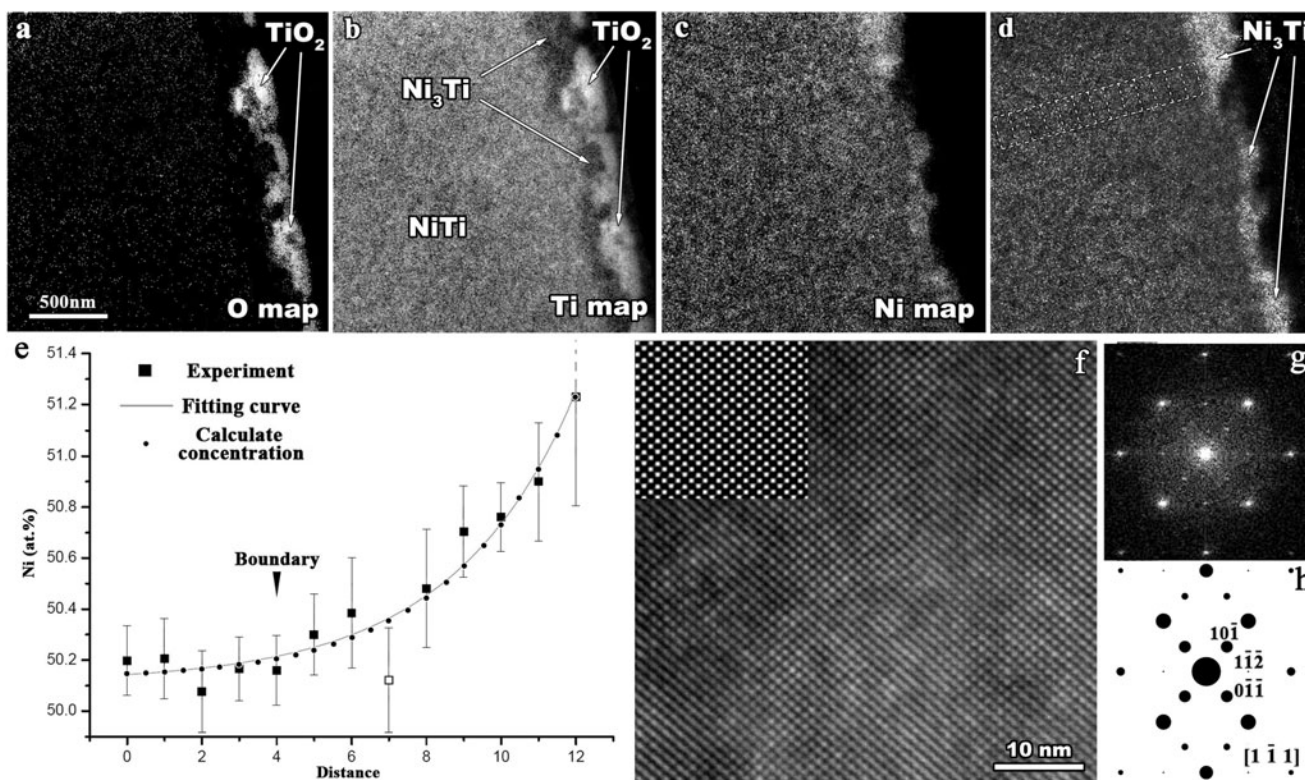
Figure 5. Low-magnification EFTEM elemental maps of (**a**) O, (**b**) Ti, and (**c**) Ni. (**d**) Ni/Ti ratio map. (**e**) Averaged Ni content in the Ni-Ti microwire close to the surface as measured from the profile of the Ni/Ti ratio map of **d** (filled squares) plus fitted exponential function (small points, equation (1)) (the Ni$_3$Ti layer starts about 100 nm further to the right of the last data point). (**f**) HRTEM image of a Ni$_3$Ti particle in Ni-rich area including simulated image; (**g**) FFT of **f**; (**h**) simulated diffraction pattern of Ni$_3$Ti $[1\bar{1}1]$ zone axis.

Electron Energy-Loss Spectroscopy and Energy-Filtered TEM

Energy-filtered TEM (EFTEM) elemental maps shown in Figure 5a–c confirm the surface layer is predominantly Ti

and O, and the bulk is predominantly Ni and Ti. The Ni/Ti ratio map obtained from the respective EFTEM maps (Fig. 5d) agrees qualitatively with the EDXS and EELS analysis described above. Figure 5e shows the profile of the

averaged Ni content across the bulk using an averaging rectangle of 125×250 nm^2 as indicated in Figure 5d. From this figure it is again seen that the Ni content increases slowly from the bulk toward the surface. The position of the B2-B19′ boundary is indicated by a black arrowhead. Below the boundary, the composition remains approximately constant. The location with the highest amount of Ni measured in this area contains 51.23 ± 0.42 at.% Ni. Here it should be mentioned that the data point with a strong deviation from the other points (indicated by an open square in Fig. 5e) corresponds to a position where a grain of B19′ martensite is observed inside the B2 shell.

Furthermore, an extra intermediate Ni-rich layer is apparent at the bulk-oxide interface with protrusions clearly matching the discontinuities in the oxide layer, as shown in Figure 5b,d. EDXS indicates that the composition of grains of this layer is close to Ni$_3$Ti (74.1 at.% Ni and 25.9 at.% Ti, ± 0.8 at.%). Figure 5f shows an HRTEM image of a particle in the Ni-rich area with the FFT shown in Figure 5g. The upper-left corner of Figure 5f shows a simulated HRTEM image (th. = 50 nm, def. = −40 nm) while in Figure 5h an electron diffraction pattern is simulated, both obtained using the Ni$_3$Ti hexagonal unit cell with space group P6$_3$/mmc with $a = 0.5096$ nm and $c = 0.8304$ nm and fitting the experimental data well.

DISCUSSION

In the present work, the microstructure of the near surface and interior of a cold-rolled Ni-Ti microwire are investigated by various TEM techniques. As expected, a native, Ti-rich oxide layer is formed during the cold-drawing process yielding a relatively smooth surface, although some cracks in the oxide can be recognized from the SEM images in Figure 1a,b. EELS and ELNES measurements reveal that the oxide contains TiO as well as TiO$_2$ grains, which can be concluded from elemental ratios and the fine structure of the ionization edges. The latter and HRTEM (not shown here) also indicate that the TiO$_2$ is of the rutile type, which confirms earlier results. In this naturally grown oxide layer, it can be expected that when exposed to atmosphere the first structure that forms is TiO, which is then gradually replaced by the more stable TiO$_2$ (Firstov et al., 2002). Only a very small concentration of Ni (<5 at.% Ni and depending on the point of detection) is measured in this layer.

As the starting alloy composition is Ni$_{49.48}$Ti$_{50.52}$, the expected martensitic start temperature is around 65°C. Hence, we expect the bulk of the wire to be the martensitic phase, as observed, although both analytical methods yield a slightly higher Ni content for the central bulk part. However, the observations also reveal a 1 μm austenite B2 shell between the core martensite and the oxide. Although the effects of the cold-rolling should not be neglected, the analytical data show that the formation of the Ti-rich oxide

layer leaves a Ni-rich shell in the metal. Because the martensitic transformation start temperature M_s is extremely dependent on the composition and decreases with increasing Ni content, M_s has dropped below room temperature in the Ni-rich shell. Considering the temperature dependence of M_s published by Tang et al. (1999), M_s drops below room temperature at $\sim$50.3 at.% Ni, which agrees with the measured values of 50.3 ± 0.3 at.% Ni from EDXS and 50.20 ± 0.14 at.% Ni from EELS. In other words, this phenomenon is clearly reproduced and confirmed by the use of two independent techniques applied to different areas of the sample. Possible artifacts in the EDXS and EELS quantification due to thickness effects have been minimized by using flat areas found via the log-ratio or by using data from Ni/Ti ratio maps.

Because it is likely that diffusion plays an important role in the final concentration gradients, an attempt was made to fit an exponential function through the experimental EELS data of the Ni concentration as seen in Figure 5e and shown in equation (1) (with r_0 being equal to 0 in Fig. 5e):

$$f(r) = a \cdot \exp[(r - r_0)/c] + b$$

$$(a = 0.03443, b = 50.10, c = 429.4). \qquad (1)$$

In between the oxide layer and the bulk, a further Ni enriched layer is detected by EFTEM. This layer is not a continuous layer and consists of Ni$_3$Ti particles (space group: hexagonal P6$_3$/mmc; lattice parameters: $a = 0.5096$ nm, $c = 0.8304$ nm). In some cases, such particles have also been observed inside the oxide layer, where they could explain part of the measured Ni signal, but mostly they are positioned in between the oxide and the bulk. Ni$_3$Ti precipitation on the edges of a wire was recently also observed by Zhang et al. on a much larger scale in intentionally oxidized macroscopic Ni-Ti. In that case the Ni$_3$Ti phase was precipitated from a eutectic liquid NiTi to NiTi + Ni$_3$Ti, which is caused by the Ni-enrichment due to the selective oxidation of Ti at high temperatures (Zhang et al., 2007). In that article, however, no Ni gradient underneath the Ni$_3$Ti region was measured.

Based on the above results, it should be possible to correlate the thickness of the Ti-depleted region, the Ni$_3$Ti layer and the oxide layer, in a similar way as was done for the Ni-depleted region in the matrix around Ni$_4$Ti$_3$ precipitates in annealed Ni-Ti bulk material (Yang et al., 2005). In equation (2), using cylindrical coordinates with r the radial distance from the center of the microwire to the surface, $C(r)$ the concentration, $\rho(r)$ the atom density per unit volume, and L_0 the unit length along the axis of the microwire, the concentration balance $\sum_{i=1,2,3}$ Ni $\cong \sum_{i=1,2,3}$ Ti is expressed assuming a 50:50 ratio for Ni and Ti. In this expression part I ($i = 1$) corresponds to the Ti depleted layer, part II ($i = 2$) corresponds to the Ni$_3$Ti layer, and part III ($i = 3$) to the oxide layer, respectively (with an assumed

zero concentration of Ni for simplicity because only very little Ni is found in the oxide layer). In the last part, $R(r)$ is the ratio TiO/TiO$_2$ in the oxide layer.

Thus,

$$\sum_{i=1,2,3} \int_i C_{Ni}(r) \cdot \rho_i(r) \cdot 2\pi r \cdot L_0 \cdot dr$$

$$\cong \sum_{i=1,2,3} \int_i C_{Ti}(r) \cdot \rho_i(r) \cdot 2\pi r \cdot L_0 \cdot dr, \qquad (2)$$

Part I: $C_{Ni}(r) = f(r); C_{Ti}(r) = 1 - f(r), \ i = 1,$

Part II: $C_{Ni}(r) = \dfrac{3}{4}; C_{Ti}(r) = \dfrac{1}{4}, \ i = 2,$

Part III: $C_{Ni}(r) = 0; C_{Ti}(r) = \dfrac{1}{2} R(r) + \dfrac{1}{3}[1 - R(r)], \ i = 3.$

Part I is fully determined as seen from equation (1), so the balance remains to be determined between the oxide and Ni$_3$Ti layers. Assuming an average oxide thickness of 200 nm, the amount of Ti missing in the Ti depleted metallic shell only accounts for up to 8% of the Ti appearing in the oxide layer. In other words, the Ni-rich Ni$_3$Ti layer is an inevitable feature for the present wires showing a Ti-oxide layer a few hundred nanometers thick. The actual thickness of the Ni$_3$Ti layer of course depends on this oxide thickness and the TiO/TiO$_2$ ratio ($R(r)$). In practice, the thickness of the Ni$_3$Ti layer will be between 120 nm for a 200 nm oxide layer containing 100% TiO and 550 nm for a 200 nm oxide layer containing 100% TiO$_2$, i.e., values in the range of the particle size observed in Figure 5a,b. Moreover, it can be expected that the size variation of the particles in the intermetallic Ni$_3$Ti layer will be due to the level of oxidation in the surface immediately above the respective grains.

Furthermore, the profile of Ni concentration shown in Figure 5e can be related to a partial erfc-like profile starting at the bottom end of the Ni$_3$Ti layer. The Ni concentration variation in Part I can indeed be considered as the result of diffusion of remaining excess Ni atoms from the intermetallic Ni$_3$Ti layer into the bulk, at least at those places where the Ni$_3$Ti layer is continuous. The concentration distribution C can be described as a function of time t and position x, as shown in equation (3):

$$C(x,t) = C_0 + (C_s - C_0)\left[1 - \mathrm{erf}\left(\frac{x}{2\sqrt{(Dt)}}\right)\right], \qquad (3)$$

$$\mathrm{erf}(\beta) = \frac{2}{\sqrt{\pi}} \int_0^\beta \exp(-\beta^2)\, d\beta, \quad \beta = \frac{x}{2\sqrt{(Dt)}}, \qquad (4)$$

where $\mathrm{erf}(x/2\sqrt{(Dt)})$ is called the error function of $(x/2\sqrt{(Dt)})$, D is the diffusion coefficient in dimensions (m^2 s^{-1}) (in this case D is constant, independent of position and concentration but depending on temperature, viscosity, and size of particles (Cahn & Haasen, 1983)), C_s is the Ni concentration (75.00 at.%) in the Ni$_3$Ti layer, and C_0 is the Ni concentration (50.10 at.%) far away beneath the B2-B19′ boundary in the bulk. Because D and t have not been measured during the process of cold working, we select $\beta = x/2\sqrt{(Dt)}$ as a variable here. The calculated diffusion profile of the Ni concentration in the relevant area is indicated by black points as shown in Figure 5e (Ni at.% between 50.14 and 51.23 at.%). The calculated result matches both the fitting curve and experimental data well and yields a value for Dt equal to 7.43×10^{-9} cm^2. Assuming a typical annealing between the steps of the cold-drawing procedure of about 10 to 20 min, this results in a diffusion coefficient D between 1.23×10^{-11} and 6.19×10^{-12} cm^2/s that are of the same order as previous measurements (Bernardini et al., 2003). So, the phenomenon of Ni concentration variation beneath the Ni$_3$Ti layer down to the bulk (in Part I) can indeed be explained by Ni diffusion from Ni$_3$Ti layer into the bulk. Moreover, the measured composition of 51.23 at.% Ni underneath the Ni$_3$Ti layer could possibly be used to estimate the annealing temperature used during intermediate heat treatments. According to the phase diagram (Okamoto & Massalski, 2000), the two-phase region (B2 - Ni$_3$Ti) that is reached at this interface with the present composition implies that a temperature of around 740°C was reached during the intermediate heat treatments of the microwire processing. This may provide a method for reverse engineering. In view of the material preparation, however, it should be remarked that the cold-working will introduce a great amount of defects, especially in the near-surface area. During plastic deformation, point defects such as vacancies are created by dislocation interactions (Wintenberger, 1959; Gonzales et al., 1975), and the diffusion can be accelerated from these defects even at intermediate temperatures.

Inside the martensite region, multiple twins are observed. Although a thorough study still has to be performed, it is clear that many different types of twins and other defects exist. Within the single image presented here in Figure 2c, three different types of twins are observed, plus severely bent lattice planes. Two compound (001) and (20$\bar{1}$) twin cases are identified, which are typical deformation twins in Ni-Ti (Otsuka & Ren, 2005). As a result of the introduction of these compound twins in between the major planar defects running from the lower-left to upper-right corner in Figure 2c, no exact orientation relationship, as expected from the symmetry-breaking martensitic transformation, could be determined in this area. In other parts of the sample (not shown), the classic (111) Type I twins of Ni-Ti martensite were observed (Nishida et al., 1995).

The above-described structural features are of great importance for medical applications of these Ni-Ti microwires. The spontaneously grown oxide layer, which can be

tuned by careful thermal treatments, hinders the release of Ni, although the importance and the exact distribution of the few percent of Ni inside this layer still has to be determined. Also, it is still not known whether or not the Ni_3Ti intermediate layer has any effect on the bonding between the oxide layer and the metal. As for the shape memory and superelasticity, although only 2% of the full diameter is an austenitic shell, differences in stress-strain behavior between the two different regions or local stress concentrations could possibly deteriorate the long-term functional properties of the material, although such predictions are still rather speculative. The heavy cold deformation also seems to have caused a large amount of twins in the B19′ martensite. How far those twins hamper or favor the martensitic transformation after cold working is another important question for further study.

CONCLUSIONS

The microstructure of an as-received Nitinol microwire was investigated by different TEM techniques. Site-specific samples were prepared by FIB. EDXS and EELS reveal that the surface oxide is predominantly Ti and O (with less than 5 at.% inhomogeneously distributed Ni). ELNES and SAED of this layer revealed it is a combination of TiO and rutile TiO_2. Due to the formation of the oxide layer a 1 μm thick shell consisting primarily of B2 is formed. In between the metallic wire and the oxide surface, an interfacial layer containing Ni_3Ti particles is observed. The maximum Ni content measured in the bulk but close to the Ni_3Ti may yield information as to which temperature was employed for annealing, due to the local Ni-enrichment as a consequence of Ti-oxidation. The 30% cold-work process leading to the micro dimensions of the wire, resulted in bending of lattice planes and twins of the B19′ martensite as seen by HRTEM.

ACKNOWLEDGMENTS

REFERENCES

BAYER, R. & ROGUIN, A. (1997). Early and late results of self-expandable Nitinol stets: Interim report from multicenter European study. *J Interven Cardiol* **10**, 207–213.

BERGER-GORBET, M., BROXUP, B., RIVARD, C. & YAHIA, L. (1996). Biocompatibility testing of NiTi screws using immunohisto-chemistry of section containing metallic implants. *J Biomed Mater Res* **32**, 243–248.

BERNARDINI, J., LEXCELLENT, C., DARÓCZI, L. & BEKE, D.L. (2003). Ni diffusion in near-equiatomic Ni-Ti and Ni-Ti(-Cu) alloys. *Philosoph Mag* **83**, 329–338.

BRYDSON, R., SAUER, H. & ENGEL, W. (1991). Probing Materials Chemistry Using ELNES in TMS Annual Meeting, New Orleans, p. 131.

BRYDSON, R., SAUER, H., ENGEL, W., THOMAS, J.M., ZEITER, E., KOSUGI, N. & KUROBA, H. (1989). Electron-energy loss and X-ray absorption-spectroscopy of rutile and anatase—A test of structural sensitivity. *J Phys: Condens Matter* **1**, 797–812.

CAHN, R.W. & HAASEN, P. (Eds.) (1983). *Physical Metallurgy* (3rd revised, enlarged ed., Parts 1 and 2). Amsterdam: North-Holland Physics Publishing.

CISSE, O., SAVAGODO, O., WU, M. & YAHIA, L. (2002). Effect of surface treatment of NiTi alloy on its corrosion behavior in Hank's solution. *Biomed J Mater Res* **61**, 339–345.

CLARKE, B., CARROLL, W., ROCHEV, Y., HYNES, M., BRADLEY, D. & PLUMLEY, D. (2006). Influence of Nitinol wire surface treatment on oxide thickness and composition and its subsequent effect on corrosion resistance and nickel ion release. *J Biomed Mater Res* **79A**, 61–70.

EGERTON, R.F. (1996). *Electron-Loss Spectroscopy in the Electron Microscope*. New York: Plenum/Springer.

FIRSTOV, G.S., VITCHEV, R.G., KUMAR, H., BLANPAIN, B. & VAN HUMBEECK, J. (2002). Surface oxidation of NiTi shape memory alloy. *Biomaterials* **23**, 4863–4871.

GONZALES, R., PIQUERAS, J. & BRU, L.I. (1975). Formation of point-defect clusters during first cycles of copper fatigues. *Phys Stat Sol* **29**, 161–166.

KOBAYASHI, Y., HONDA, Y., CHRISTIE, L., TEIRSTEN, P., BAILEY, S., BROWN, C., MATTHEWS, R., FRANCO, A., SCHWARTZ, R., GOLDBERG, S., POPMA, J., YOCK, P. & FITZGERALD, P. (2001). Long-term vessel response of self-expending coronary stent: A serial volumetric intravascular ultrasound analysis from the ASSURE trial. *J Am College Cardiol* **37**, 1329–1334.

KOBAYASHI, S., OHGOE, Y., OZEKI, K., SATO, K., SUMIYA, T. & HIRAKURI, K. (2005). Diamond-like carbon coatings on orthodontic archwires. *Diamond Related Mater* **14**, 1094–1097.

KUJALA, S., PAJALA, A., KALLIOINEN, M., PRAMILA, A., TUUKKANEN, J. & RYHÄNEN, J. (2004). Biocompatibility and strength properties of nitinol shape memory alloy suture in rabbit tendon. *Biomaterials* **25**, 353–358.

MICHIARDI, A., APARICIO, C., PLANELL, J. & GIL, F. (2006). New oxidation treatment of NiTi shape memory alloys to obtain Ni-free surfaces and to improve biocompatibility. *J Biomed Mat Res* **77B**, 249–256.

NISHIDA, M., YAMAUCHI, K., ITAI, I., OHGI, H. & CHIBA, A. (1995). High-resolution electron-microscopy studies of twin boundary structures in B19′ martensite in the Ti-Ni shape-memory alloy. *Acta Metall Mater* **43**, 1229–1234.

OKAMOTO, H. & MASSALSKI, T.B. (2000). Impossible and improbable forms of binary phase diagrams. In *Desk Handbook: Phase Diagrams for Binary Alloys*, Okamoto, H. (Ed.), pp. xxxix–xliii. Materials Park, OH: ASM International.

OTSUKA, K. & REN, X. (2005). Physical metallurgy of Ti-Ni-based shape memory alloys. *Prog Mater Sci* **50**(5), 511–678.

POTAPOV, P.L. & SCHRYVERS, D. (2004). Measuring the absolute position of EELS ionisation edges in a TEM. *Ultramicroscopy* **99**, 73–85.

POTAPOV, P.L., TIRRY, W., SCHRYVERS, D., SIVEL, V.G.M., WU, M.Y., ASLANIDIS, D. & ZANDBERGEN, H. (2007). Cross-section transmission electron microscopy characterization of the near-surface structure of medical Nitinol superelastic tubing. *J Mater Sci: Materials for Medicine* **18**, 483–492.

ROGUIN, A., GRANADIER, E., LINN, S., MARKIEWICZ, W. & BEYER, R. (1999). Continued expansion of Nitinol self-expandable stent angiographic analysis and 1-year clinical follow-up. *Am Heart J* **138**(2), 326–333.

RYHÄNEN, J. (1999). In *Biocompatibility Evaluation of Nickel-Titanium Shape Memory Metal Alloy*. Ph.D. Thesis, Oulu University, Finland.

RYHÄNEN, J., NIEMI, E., SERLO, S., NIEMELÄ, E., SANDVIK, P., PERNU, H. & SALO, T. (1997). Biocompatibility of nickel-titanium metal and its corrosion behaviour in human cell cultures. *J Biomed Mater Res* **35**, 451–457.

SHABALOVSKAYA, S.A. (1996). On the nature of the biocompatibility and on medical applications of NiTi shape memory and superelastic alloys. *Bio-Med Mater Eng* **6**, 267–289.

SHABALOVSKAYA, S.A. (2001). Physicochemical and biological aspects of Nitinol as a biomaterial. *Int Mater Rev* **46**, 233–250.

SHABALOVSKAYA, S.A. (2002). Surface, corrosion and biocompatibility aspects of Nitinol as an implant material. *Bio-Med Mater Eng* **12**, 69–109.

SUI, J. & CAI, W. (2006). Effect of diamond-like carbon (DLC) on the properties of the NiTi alloys. *Diamond Related Mater* **15**, 1720–1726.

TAKESHITA, F., TAKATA, H., AYUKAWA, Y. & SUETSUGU, T. (1997). Histomorphometric analysis of the response of rat tibia to shape memory alloy (Nitinol). *Biomaterials* **18**, 21–25.

TANG, W., SUNDMAN, B., SANDSTRÖM, R. & QIU, C. (1999). New modelling of the B2 phase and its associated martensitic transformation in the Ti-Ni system. *Acta Mater* **47**, 3457–3468.

WEVER, D., VELDERHUIZEN, A., VRIES, J.D., BUSSCHER, H., UGES, D. & VAN HORN, J. (1998). Electrochemical and surface characterization of NiTi alloy. *Biomaterials* **19**, 761–769.

WINTENBERGER, M. (1959). Elimination des lacunes dans les aluminiums tres purs. *Acta Metall* **7**, 549–555.

YANG, Z.Q., TIRRY, W. & SCHRYVERS, D. (2005). Analytical TEM investigations on concentration gradients surrounding Ni_4Ti_3 precipitates in Ni-Ti shape memory material. *Scripta Mat* **52**, 1129–1134.

ZHANG, J., FAN, G., ZHOU, Y., DING, X., OTSUKA, K., NAKAMURA, K., SUN, J. & REN, X. (2007). Does order–disorder transition exist in near-stoichiometric Ti–Ni shape memory alloys? *Acta Mater* **55**, 2897–2905.